



ELSEVIER

Contents lists available at ScienceDirect

Planetary and Space Science

journal homepage: www.elsevier.com/locate/pss

Electron transport and precipitation at Mercury during the MESSENGER flybys: Implications for electron-stimulated desorption

David Schriver^{a,*}, Pavel Trávníček^{c,d}, Maha Ashour-Abdalla^{a,b}, Robert L. Richard^a, Petr Hellinger^d, James A. Slavin^e, Brian J. Anderson^f, Daniel N. Baker^g, Mehdi Benna^h, Scott A. Boardsen^e, Robert E. Gold^f, George C. Ho^f, Haje Korth^f, Stamatios M. Krimigis^{f,i}, William E. McClintock^g, Jason L. McLain^j, Thomas M. Orlando^j, Menelaos Sarantos^f, Ann L. Sprague^k, Richard D. Starr^l^a Institute of Geophysics and Planetary Physics, University of California, Los Angeles, CA 90095-1567, USA^b Department of Physics and Astronomy, University of California, Los Angeles, CA 90095-1567, USA^c Space Sciences Laboratory, University of California, Berkeley, CA 94720-7450, USA^d Astronomical Institute, ASCR, 14131 Prague, Czech Republic^e Heliophysics Science Division, NASA Goddard Space Flight Center, Greenbelt, MD 20771, USA^f Johns Hopkins University Applied Physics Laboratory, Laurel, MD 20723, USA^g Laboratory for Atmospheric and Space Physics, University of Colorado, Boulder, CO 80303, USA^h Solar System Exploration Division, NASA Goddard Space Flight Center, Greenbelt, MD 20771, USAⁱ Academy of Athens, Office of Space Research Technology, Athens 11527, Greece^j School of Chemistry and Biochemistry and School of Physics, Georgia Institute of Technology, Atlanta, GA 30332, USA^k Lunar and Planetary Laboratory University of Arizona, Tucson, AZ 85721, USA^l Physics Department, The Catholic University of America, Washington, DC 20064, USA

ARTICLE INFO

Article history:

Received 29 July 2010

Received in revised form

8 March 2011

Accepted 17 March 2011

Available online 1 April 2011

Keywords:

Mercury

Magnetosphere

Numerical simulations

Electron transport

Electron-stimulated desorption

MESSENGER

ABSTRACT

To examine electron transport, energization, and precipitation in Mercury's magnetosphere, a hybrid simulation study has been carried out that follows electron trajectories within the global magnetospheric electric and magnetic field configuration of Mercury. We report analysis for two solar-wind parameter conditions corresponding to the first two MESSENGER Mercury flybys on January 14, 2008, and October 6, 2008, which occurred for similar solar wind speed and density but contrasting interplanetary magnetic field (IMF) directions. During the first flyby the IMF had a northward component, while during the second flyby the IMF was southward. Electron trajectories are traced in the fields of global hybrid simulations for the two flybys. Some solar wind electrons follow complex trajectories at or near where dayside reconnection occurs and enter the magnetosphere at these locations. The entry locations depend on the IMF orientation (north or south). As the electrons move through the entry regions they can be energized as they execute non-adiabatic (demagnetized) motion. Some electrons become magnetically trapped and drift around the planet with energies on the order of 1–10 keV. The highest energy of electrons anywhere in the magnetosphere is about 25 keV, consistent with the absence of high-energy (> 35 keV) electrons observed during either MESSENGER flyby. Once within the magnetosphere, a fraction of the electrons precipitates at the planetary surface with fluxes on the order of $10^9 \text{ cm}^{-2} \text{ s}^{-1}$ and with energies of hundreds of eV. This finding has important implications for the viability of electron-stimulated desorption (ESD) as a mechanism for contributing to the formation of the exosphere and heavy ion cloud around Mercury. From laboratory estimates of ESD ion yields, a calculated ion production rate due to ESD at Mercury is found to be on par with ion sputtering yields.

© 2011 Elsevier Ltd. All rights reserved.

1. Introduction

Mercury, the closest planet to the Sun, has the distinction of having the smallest planetary magnetosphere in our solar system (Kivelson and Russell, 1995). Mariner 10 data from the 1970s

established that Mercury has an intrinsic magnetic field, and this inference has been confirmed by magnetic field observations by the Mercury Surface, Space Environment, Geochemistry, and Ranging (MESSENGER) spacecraft. The planet has a dipole moment of $\sim 250 \text{ nT } R_M^3$ (where R_M is Mercury's radius, or 2440 km) and a tilt with respect to the planetary rotation axis of no more than 5° (Ness et al., 1974, 1975, 1976; Jackson and Beard, 1977; Whang, 1977; Anderson et al., 2008). The solar wind interaction with Mercury's intrinsic magnetic field creates a

* Corresponding author. Tel.: +1 310 825 6843; fax: +1 310 206 3051.
E-mail address: dave@igpp.ucla.edu (D. Schriver).

magnetosphere that can divert solar wind plasma around the planet and act as a (leaky) shield, in a manner similar to Earth's magnetosphere. In contrast to Earth, however, Mercury has almost no atmosphere or ionosphere, and plasma within the magnetosphere can precipitate directly onto the planetary surface. Due to the relatively weak intrinsic planetary magnetic moment and the highly varying, relatively high-pressure solar wind, the magnetosphere of Mercury is the most dynamic one in the solar system (e.g., Russell et al., 1988). The Mariner 10 spacecraft passes through Mercury's magnetosphere showed extreme changes in the magnetic field occurring on timescales of a few minutes (Ness et al., 1974), and recent MESSENGER observations show evidence of rapid and extreme loading and unloading of magnetic flux within Mercury's magnetosphere, most likely due to magnetic reconnection (Slavin et al., 2010).

The MESSENGER flybys of Mercury in 2008 and 2009 have revealed many interesting new results concerning the planet's magnetosphere and exosphere (Solomon et al., 2008). One of the more puzzling results has been the complete lack of magnetospheric energetic electrons with energies above 35 keV, although there was evidence from MESSENGER's X-Ray Spectrometer (XRS) of ~ 10 keV electrons near the planet (Ho et al., this issue). This result is in contrast to Mariner 10 data, which showed evidence of high-energy (> 35 keV) electron bursts during its March 1974 encounter (Simpson et al., 1974). Possibly related to this lack of energetic electrons is that although MESSENGER did pass through Mercury's magnetosphere when it was undergoing rapid changes in response to an oscillating interplanetary magnetic field (IMF) north–south component (Slavin et al., 2010), the solar wind during all of the flybys would be considered “quiet” since the encounters occurred during solar minimum, with relatively low, steady solar wind pressure (Baker et al., this issue).

In addition to its magnetosphere, Mercury has a tenuous, collisionless, neutral, and ionized exosphere with neutrals H, He, Na, K, and Ca that were originally observed spectroscopically (Broadfoot et al., 1976; Potter and Morgan, 1985; Bida et al., 2000) and with Mg and Ca^+ discovered by the Mercury Atmospheric and Surface Composition Spectrometer (MASCS) onboard the MESSENGER spacecraft (McClintock et al., 2008, 2009; Vervack et al., 2010). Other ions have been confirmed *in situ* by direct measurements made by the Fast Imaging Plasma Spectrometer (FIPS), also onboard MESSENGER (Zurbuchen et al., 2008). A variety of processes have been commonly cited as mechanisms that can populate the exosphere with neutrals and ions, including photo-sputtering, thermal desorption, ion sputtering, and meteoroid impact (Hunten et al., 1988; Morgan and Killen, 1997; Killen and Ip, 1999; Potter et al., 1999; Miliillo et al., 2005; Domingue et al., 2007). Prior to the MESSENGER flybys, ground-based observations of moderately volatile species (e.g., Na and K) pointed to a picture in which thermal and solar-radiation processes act on the sunlit surface to release material to the exosphere continuously, whereas sputtering by precipitating solar-wind ions, modulated by the planet's magnetic field, provide spatial and temporal variability (Sprague et al., 1997; Killen et al., 2001; Leblanc et al., 2003; Kallio et al., 2008). The recent observations provided during the MESSENGER flybys, however, show that these mechanisms alone cannot account for the distribution and abundances of neutral species such as Na, Mg, Ca, and Ca^+ (Vervack et al., 2010). A somewhat overlooked but possibly very important process that may help explain the observations is electron-stimulated desorption (ESD), which through electron precipitation onto Mercury's planetary surface can release neutrals and ions into the space environment (Madedy et al., 1998; Orlando et al., 2010; Vervack et al., 2010; McLain et al., 2011).

To examine electron transport and energization within Mercury's magnetosphere and also to determine electron precipitation

fluxes during the MESSENGER flybys, a simulation study has been carried out that follows electron trajectories within the global electric and magnetic field configuration of Mercury. For the most part, electron motion in the solar wind and within a planetary magnetosphere is adiabatic, but it has been shown that near regions of weak magnetic field and/or highly curved field lines near reconnection regions or very thin current sheets, electrons can become demagnetized and the guiding-center approximation breaks down, resulting in non-adiabatic motion and direct acceleration by electric fields that are present locally (Spieser, 1965; Dungey, 1989; Lyons and Pridmore-Brown, 1990, 1992; Schriver and Ashour-Abdalla, 1994, 1995). It has been shown that near a magnetotail reconnection site in the Earth's global magnetospheric fields a combination of non-adiabatic (demagnetization) and adiabatic motion can accelerate cool lobe electrons with initial energies from ~ 50 eV up to plasma sheet energies (\sim keV) and also result in field-aligned beams and power-law velocity distributions (Schriver et al., 1998). Since Mercury's overall magnetic field is relatively weak compared to Earth's and since it has been established that reconnection is occurring at Mercury (e.g., Slavin et al., 2009, 2010), it is expected that non-adiabatic motion will play an important role in electron acceleration and transport. To follow tens of thousands of electron trajectories in a global magnetospheric field configuration and remain computationally feasible, a code that switches between guiding center and full particle motion has been developed (Schriver et al., 1998, 2005). The global electric and magnetic field configuration that describes the solar wind interaction with Mercury's magnetosphere is taken from a self-consistent three-dimensional global hybrid simulation, which provides the most realistic field model presently available (Trávníček et al., 2009, 2010).

The electron modeling study here has been carried out for two solar-wind parameter conditions that correspond closely to the conditions that occurred during MESSENGER's first two Mercury flybys on January 14, 2008 (M1), and October 6, 2008 (M2). The solar wind parameters during the two flybys were very similar in terms of solar wind speed and density, except for one crucial difference: during M1 the IMF had a northward component, while during M2 the IMF was southward. The IMF for both flybys also had a large radial (anti-sunward) component. The direction of the IMF either northward or southward has a strong influence on where magnetic reconnection will occur on the dayside and nightside regions; for example, when the IMF is northward, dayside reconnection occurs at high latitudes, whereas for southward IMF reconnection occurs more equatorward on the dayside and in the magnetotail on the nightside. Hybrid simulations have been carried out for the two flyby situations (Trávníček et al., 2009, 2010), and the electron trajectories are traced within the fields taken from these simulations. The main results found from this study show that some solar wind electrons follow complex trajectories near to or where dayside reconnection is occurring and enter the magnetosphere at these locations. The entry locations depend on the solar wind IMF (north or south), and when moving through the entry regions, electrons are energized via non-adiabatic (demagnetized) motion. Once within the magnetosphere, a fraction of the electrons precipitates with fluxes on the order of $10^9 \text{ cm}^{-2} \text{ s}^{-1}$ and energies of hundreds of eV. This finding has important implications for the viability of ESD as a mechanism for contributing to the formation of the exosphere and heavy ion cloud around Mercury. Recent results of the ion yield due to electron bombardment of simulated Mercury regolith targets (McLain et al., 2011), combined with the precipitation rate of electrons calculated here, show that ESD can contribute ions off the planet at a rate comparable to ion sputtering rates determined by Killen et al. (2004). Some electrons also can become trapped and drift around the planet, with energies on

the order of 1–10 keV, which compares well with MESSENGER XRS observations of electrons with similar energies (Ho et al., [this issue](#)). In general the simulation results show that the highest energy of electrons anywhere in the magnetosphere under conditions similar to those of the encounters was about 25 keV, which is consistent with the absence of high-energy electrons observed during the MESSENGER flybys (Ho et al., [this issue](#)).

The outline of the paper is as follows. In Section 2, a description of the simulation model and the initial parameters used are provided. In Section 3, results are presented from the electron trajectory tracing simulations. Summary and conclusions complete the paper in Section 4.

2. Simulation model

Two simulation techniques have been combined to examine electron transport in Mercury's magnetosphere. One is a particle trajectory tracing code to follow electron kinetics, and the other is a hybrid simulation model that provides the global electric and magnetic field configuration through which the electron trajectories are followed. The two simulation techniques are now described.

2.1. Hybrid simulation model

The electric and magnetic field configurations of Mercury's magnetosphere through which the electron trajectories are followed are taken from the results of a three-dimensional global hybrid simulation code. Hybrid codes self-consistently describe the dynamics of collisionless plasmas with ions treated as kinetic particles and isothermal electrons considered as a massless fluid (e.g., Winske, 1985; Matthews, 1994; Lipatov, 2002; Winske et al., 2003). Hybrid code technology has matured since the initial application of one-dimensional simulations for space plasma physics problems in the vicinity of the Earth's bow shock (Leroy et al., 1981, 1982), and has been used to study a variety of problems, including processes in the upstream bow shock (Winske and Leroy, 1984; Hada and Kennel, 1985), Earth's magnetopause (Swift and Lee, 1983) and magnetosphere (Omura et al., 1985; Tanaka, 1985; Swift, 1995), reconnection in Earth's magnetotail (Krauss-Varban and Omidi, 1995; Hesse et al., 1995; Lin and Swift, 1996; Kuznetsova et al., 1996), and instabilities due to non-gyrotropic distribution functions (Convery et al., 2002). Multi-dimensional hybrid modeling on a global scale has been used to examine the interaction between solar wind flow and such solar system bodies as Venus, Mars, Pluto, comets, and asteroids (Brecht, 1990, 1997; Brecht et al., 1993; Dubinin et al., 1996, 1998; Lipatov et al., 1997, 2002; Shimazu, 1999, 2001; Blanco-Cano et al., 2003; Delamere and Bagenal, 2004; Delamere, 2009).

The hybrid code to be used for this study is based on the Current Advance Method and Cyclic Leapfrog (CAM-CL) algorithms developed by Matthews (1994) and is fully parallelized. A three-dimensional version of the code with parameters used to model the solar wind interaction with Mercury's magnetosphere has been described in detail by Trávníček et al. (2007, 2009, 2010). In this study the results are taken from simulation runs that correspond to the first two MESSENGER flybys as described by Trávníček et al. (2010). The three-dimensional hybrid simulation system size used in these runs included $594 \times 272 \times 272$ grids, which translates to a spatial size of $-10R_M < x < 4R_M$, where x is along the Sun–planet line and positive sunward; $-7.5R_M < y, z < 7.5R_M$, where y is along the dawn–dusk direction and positive toward dusk, and z is along the north–south planetary axis and positive toward north,

completing the right-handed orthogonal Mercury-centered coordinate system. It should be noted that the grid size used for these simulations resolves the ion Larmor radius and ion inertial length throughout the entire spatial domain. A complete description of the hybrid simulation code for these particular runs has been given by Trávníček et al. (2010).

Because electrons are treated as a massless fluid in the hybrid simulations, to study electron kinetics we launch thousands of individual negatively charged particles (using the code described in Section 2.2) within the magnetospheric fields taken from the hybrid simulations. Two cases are examined, corresponding approximately to the solar wind conditions during the first two MESSENGER flybys of Mercury. Table 1 lists the corresponding solar wind parameters as determined from Magnetometer (MAG) measurements made during the flybys and those inferred from the positions of the magnetopause and bow shock and from a predictive solar wind model (Baker et al., [this issue](#)). The intrinsic planetary dipole magnetic field is oriented such that magnetic north points toward geographic south, similar to the Earth's magnetic field, and in the simulations there is no dipole tilt with respect to the rotation axis. All parameters used in the two simulation cases are the same except for the orientation of the IMF, which has a northward-directed magnetic field component ($B_z > 0$) in the first case, similar to that during M1, and the second case has a southward-directed magnetic field component ($B_z < 0$), similar to that during M2. The parameters given in Table 1 are based on using a solar wind injection speed (V) from the left-hand boundary: $V = 4V_A$, where V_A is the Alfvén velocity given by $V_A = B / (4\pi nm)^{1/2}$, B is the magnetic field magnitude in the solar wind, n is the solar wind proton density, and m is the proton mass, all in Gaussian units.

2.2. Large-scale particle trajectory tracing

In large-scale particle tracing simulations, the trajectories of tens of thousands of individual charged particles are followed in a model of the electric and magnetic fields representing Mercury's magnetosphere. The behavior of individual particles can be examined to learn about the basic physics of motion for different field configurations (e.g., current sheets, reconnection regions, inductive fields). This approach has been used to understand electron acceleration near X-line reconnection regions (Schriver and Ashour-Abdalla, 1994, 1995; Smets et al., 1996; Schriver et al., 1998, 2005), during substorms (Birn et al., 1998; Delcourt et al., 2005), during storms (Hudson et al., 1996, 1999, 2000), and as a result of ultra-low-frequency waves present during storms (Elkington et al., 1999, 2003; Perry et al., 2005).

In this study we follow electron trajectories launched from the solar wind in the electric and magnetic fields described by the global hybrid simulation model of solar wind interaction with Mercury's magnetosphere discussed in Section 2.1. Starting from the solar wind source region, the equation of motion of each particle is solved using either the three-dimensional guiding center set of equations or the full particle Lorentz-force equation. In the majority of the solar wind and magnetosphere, guiding-center equations are appropriate, which is beneficial from a

Table 1
Summary of solar wind parameters used for the two simulation runs.

Solar wind parameters	Speed (km/s)	Density (cm^{-3})	Magnetic field (nT)
Simulation 1 (S1)	450	15	$ \mathbf{B} = 18; B_x = -16.7, B_y = 0, B_z = 6.7$
Simulation 2 (S2)	450	15	$ \mathbf{B} = 18; B_x = -16.7, B_y = 0, B_z = -6.7$

computational point of view since the guiding-center time step in general is much larger than the gyro-period. But it has been shown that near reconnection regions and in thin current sheets where the magnetic field is small, non-adiabatic motion is possible whereby electrons become essentially demagnetized and strong acceleration can occur (e.g., Schriver and Ashour-Abdalla, 1994, 1995); full particle motion must be resolved near these locations.

A code that switches between guiding-center and Lorentz-force equations of motion has been developed (Schriver et al., 2005) and is used here. The relativistic guiding center equations (Northrop, 1963) for transverse velocity are

$$v_{\perp} = \frac{\mathbf{E} \times \mathbf{B}}{B^2} + \frac{\mu}{q\gamma} \frac{\mathbf{B} \times \nabla B}{B^2} + \frac{p_{\parallel}^2}{q\gamma m_0} \frac{\mathbf{B} \times (\mathbf{B} \cdot \nabla) \mathbf{B}}{B^4}$$

where \mathbf{E} and \mathbf{B} are the electric and magnetic fields, respectively, μ is the magnetic moment, the relativistic factor is given by $\gamma = 1/(1-v^2/c^2)^{1/2}$, where v is the magnitude of the particle velocity and c is the speed of light, the rest mass is m_0 , the momentum parallel to the local magnetic field is p_{\parallel} , and the charge is q . The magnetic moment is assumed to be constant for adiabatic guiding-center motion and is given by $\mu = p_{\perp}^2/2m_0B$, where p_{\perp} is the momentum perpendicular to the local magnetic field. The parallel equation of motion is given by

$$\frac{dp_{\parallel}}{dt} = qE_{\parallel} - \frac{\mu}{\gamma} \nabla_{\parallel} B$$

A time centered leap-frog fourth-order predictor-corrector scheme (Press et al., 1989) is used to follow a particle's guiding center motion through the specified magnetospheric magnetic and electric fields. A variable time step (Δt) is based on local field conditions and must be smaller than any spatial gradients in the magnetic field, i.e., $\Delta t < (v_{\parallel} |\nabla_{\parallel} B|/B)^{-1}$.

It should be noted that correction terms to the above equations have been used in the particle tracing study of Perry et al. (2005), on the basis of results of Brizard and Chan (1999), to maintain higher accuracy. Our results following electrons in Earth's and Mercury's magnetosphere have shown that the Northrop (1963) equations maintain a high degree of accuracy and conserve energy to much better than 1%, and we have not included the correction terms used by Perry et al. (2005). Although the relativistic equations are maintained, in this study none of the electrons reached relativistic energies and $\gamma = 1$ can be used throughout the simulation run. Double precision is used in the calculations to ensure that round off and accumulation errors are exceedingly small over the time length of the simulation run.

When breakdown of adiabaticity occurs, for example, very close to a reconnection X-line, full particle motion is used. In this case the relativistic Lorentz-force equation is invoked:

$$m_0 \frac{d\mathbf{u}}{dt} = q\mathbf{E} + q(\mathbf{v} \times \mathbf{B})$$

where $\mathbf{u} = \gamma\mathbf{v}$, with γ the relativistic factor and m_0 the rest mass as before. Gyromotion is fully resolved, and an appropriate time step is used (i.e., $\Omega\Delta t < 0.1$, where Ω is the gyrofrequency).

To determine whether the guiding-center or Lorentz-force equation of motion should be used, the κ parameter is calculated at every time step, where $\kappa = (R/\rho)^{1/2}$ (Büchner and Zelenyi, 1986, 1989), R is the radius of curvature of the magnetic field, and ρ is the gyroradius; the latter two are both determined locally at the position of the particle. In general, when $\kappa \gg 1$, particle behavior is adiabatic. For $\kappa < 1$, particles exhibit non-adiabatic motion (Büchner and Zelenyi, 1989; Delcourt et al., 1996). When $\kappa \sim 1-5$, the particle behavior can be quite complicated, and there are several parameter dependencies that govern the motion

(e.g., Delcourt et al., 1996). In much of the Earth's magnetosphere, κ is large, ~ 50 , or more (e.g., Zelenyi et al., 1990), but as an electron nears a reconnection region or enters a thin current-sheet region, κ decreases rapidly to values < 10 , and then the particle motion can become non-adiabatic (Schriver et al., 1998). It has been found through trial and error that the switch between guiding-center motion and full particle motion should be made at a relatively high value of $\kappa \sim 20$ in order to assure a smooth, energy-conserving change between the two types of motion and their vastly different time steps (Schriver et al., 2005). Fortunately most electrons enter and leave the non-adiabatic region relatively quickly, and thus the amount of computing time spent calculating full particle motion is small. But this switching is essential to capture accurately the physics occurring in the magnetosphere. In guiding-center motion there is no gyrophase information, but the phase angle is needed when initializing full particle motion. This need is handled by assuming a random phase angle when making the switch from guiding-center to full particle motion. Experience following thousands of particles has shown that statistically the range of phases that the particles assume is randomly spread over 360° , providing full coverage of the velocity distribution function in phase angle.

The guiding center/full dynamics switching code is vital here, since the larger time steps that can be used during guiding center motion, which may be applied within most of the magnetosphere, coupled with high electron mobility (large thermal speeds), allow runs to be carried out for a sufficiently long time to follow the entry of electrons into the magnetosphere from the solar wind, and then to the magnetotail and inner magnetosphere, including multiple entries to the tail (Schriver et al., 2005). Virtual detectors placed at several locations within the magnetosphere are used to collect electron data throughout the run to calculate distribution functions and fluxes (e.g., Ashour-Abdalla et al., 1993, 1994). This is done because storing all of the particle data (e.g., three-dimensional position, velocity, κ) at each time step for tens of thousands of particles is prohibitive for reasons of file size. To keep the data sets manageable, virtual detectors are in the form of planes, spherical surfaces, or any type of surface appropriate to the region where data are desired. Using a normalization factor that depends on the solar wind speed, density, size of launch region, and number of particles launched, particle counts are converted into fluxes, densities, and velocity distribution functions at the location of the virtual detector (e.g., Richard et al., 1994).

Electrons are launched in the solar wind upstream of the bow shock, with a Maxwellian velocity distribution function characteristic of the solar wind, i.e., a 450 km/s solar wind speed in the x -direction and a three-dimensional thermal speed of 20 eV at $x = 3.0R_M$ and randomly spread in y and z over $-3.5R_M < y, z < 3.5R_M$. This geometry is illustrated schematically in Fig. 1, which shows density contours from the hybrid simulation for the case corresponding to M1 and the locations where electrons are launched into the electric and magnetic fields taken from the hybrid simulation. Electrons are followed until they hit an exterior boundary, taken to be the hybrid simulation box boundaries with $-10R_M < x < 4R_M$ and $-7.5R_M < y, z < 7.5R_M$, or the internal boundary at the surface of the planet ($r = 1R_M$ around the planetary center at the coordinate system origin).

3. Results and discussion

When electrons are launched from the upstream solar wind region for the two simulation cases with parameters given in Table 1, their motion in the solar wind is adiabatic and they move like "beads on a string" along the interplanetary magnetic field line on which they are initialized, in the sense that there is free

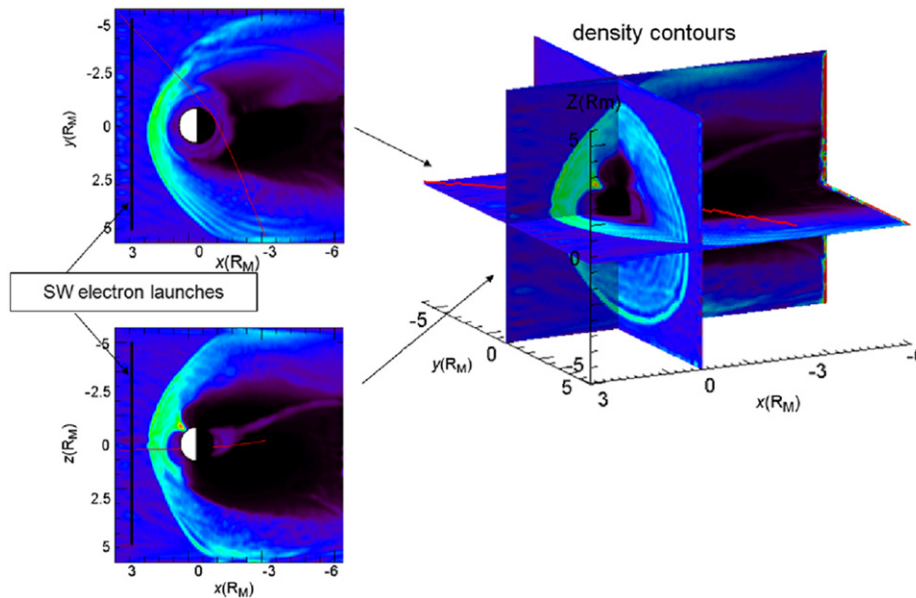


Fig. 1. Density contours from the hybrid simulation 1 in the equatorial plane (upper left), noon-midnight meridian (lower left), and the same planes in a three-dimensional representation (right panel). The Sun is to the left in each panel. The red trace in each of the contour plots shows the trajectory of the MESSENGER spacecraft during M1. Electrons are launched at $x=3R_M$, upstream of the bow shock as indicated on the left two panels.

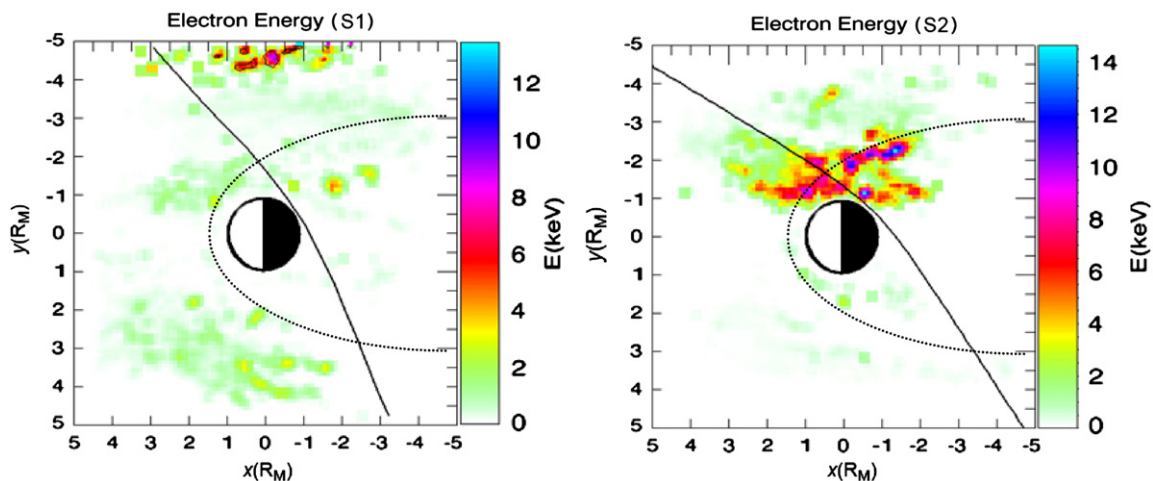


Fig. 2. Electron energy profiles in the equatorial plane are shown for simulation 1 (S1) with northward IMF on the left and simulation 2 (S2) with southward IMF on the right. The energy color scale is shown to the right of each panel, and the solid curve shows MESSENGER's trajectory for each flyby. The dotted curve shows the approximate location of the magnetopause boundary between the solar wind and the magnetosphere. The Sun is to the left in each panel.

streaming parallel to the magnetic field and particle motion transverse to \mathbf{B} is due primarily to $\mathbf{E} \times \mathbf{B}$ convection. All electrons are launched with a three-dimensional randomized Maxwellian velocity distribution (with temperature 20 eV) and move parallel to the magnetic field with whatever parallel velocity component they have initially, as well as convect with the solar wind. Because electrons have a very small mass, the electron thermal speed, v_{th} , is larger than the solar wind speed, v_{sw} (a temperature of 20 eV corresponds to $v_{th} \cong 2000$ km/s, whereas $v_{sw} = 450$ km/s), and so for most electrons their parallel velocity is larger than their transverse convection velocity. About 80% of electrons launched move more rapidly along the magnetic field line (compared to the speed of solar wind convection) and exit the system quickly either at the upstream injection boundary or at one of the downstream external boundaries without entering the magnetosphere. About

20% of electrons launched enter the magnetosphere, i.e., electrons cross the magnetopause boundary between the shocked solar wind and the region dominated by the internal planetary magnetic field, and circulate in the magnetosphere, either exiting the system downstream through the magnetotail or precipitating at the planet's surface. About 5% of total launched solar wind electrons precipitate.

3.1. Electron energies in the equatorial plane

The spatial profile and energy of electrons that enter the magnetosphere and cross the equatorial (x - y) plane virtual detector (at $z=0$) are shown in Fig. 2 for the two cases simulated. The two simulation cases will be referred to as simulation 1 (S1), which corresponds to the parameters used for M1 with

northward IMF, and simulation 2 (S2), which corresponds to the parameters used for M2 with southward IMF. In general it can be seen that for S1 (left panel) the energies are on average lower (~ 1 keV) than for S2 (right panel), where energies can be > 5 keV. Also for S2 there is a preference for higher-energy electrons on the dawn side. The differences between the two cases in terms of spatial distribution in the equatorial plane and energy are due primarily to the orientation of the IMF. For S1, which is for northward IMF, reconnection tends to occur at much higher latitudes almost over the north pole, and in general is not as efficient, whereas for southward IMF (S2), reconnection occurs at lower latitudes and is much more effective. It should be noted, however, that even for southward IMF (S2), the relatively large radial component of the IMF (B_x) alters the magnetic topology such that dayside reconnection does not occur at the equator as it would for purely southward IMF, but rather at latitudes north of the equator. The asymmetry in electron energy toward dawn for southward IMF as seen in the right panel of Fig. 2 is due to the direction of the solar-wind convection electric field, i.e., $-\mathbf{v}_{sw} \times \mathbf{B}$, which points dawn to dusk for southward IMF ($E_y > 0$), accelerating negatively charged solar wind electrons in the dawnward direction near the reconnection region that forms between the solar wind IMF and the planetary magnetic field. In addition to this process for electrons coming from the solar wind direction, any electrons in the magnetotail convecting toward the planet from the nightside will naturally drift toward dawn and around the planet due to radius of curvature and gradient B drift in the equatorial plane.

In the simulation electrons with relatively low initial parallel velocity, i.e., $v_{\parallel} < v_{sw}$, move with the solar wind and can come into contact with Mercury's magnetospheric fields. Of these electrons, the ones that pass near the dayside reconnection region between the IMF and Mercury's intrinsic magnetic field can become demagnetized, exhibiting non-adiabatic motion and crossing magnetic field lines (e.g., Schriver et al., 1998) such that they move onto planetary magnetic field lines having at least one end connected to the planet. The electrons that enter the magnetosphere in this way then become magnetized again after leaving the vicinity of the reconnection region, resuming their adiabatic, bead-on-a-string motion. Depending on the pitch angle, given by $\tan^{-1}(v_{\parallel}/v_{\perp})$, they either mirror bounce in the dipolar field for large pitch angles or, for sufficiently small pitch angles within the loss cone, they precipitate at the planetary surface.

During the transport process from the solar wind into the magnetosphere, electrons with initial energies ~ 20 eV can gain energies up to several keV, as can be seen in Fig. 2. The energization occurs in two ways. One way this happens is near the reconnection region where the electrons become demagnetized due to the low magnetic field and/or kinked magnetic field lines, and any electric fields in the region can directly accelerate the particle (Speiser, 1965; Dungey, 1989; Schriver et al., 1998). In the second way, through adiabatic betatron acceleration, electrons (after they have already entered the magnetosphere near the reconnection region) convect into a region of stronger magnetic field, and by conservation of the first adiabatic invariant ($\mu = W_{\perp}/B$), the perpendicular energy W_{\perp} increases. The energy electrons gain as they travel from the solar wind to the magnetosphere is through a combination of these two energization processes, but the precise amount of energy gained through either process is a complex dependence on particle pitch and phase angle, proximity to the reconnection region, and the end location of the particle in the magnetosphere. In the equatorial plane these processes result in energies of ~ 1 –10 keV, as seen in Fig. 2. An examination of several individual electron energy profiles reveals that on average about 70–80% of the final energy achieved for \sim keV electrons is due to acceleration near

reconnection regions, with the remaining 20–30% due to adiabatic betatron acceleration. It is important to note that in the two-step acceleration process it is acceleration near the reconnection region that provides the first kick in energy up to hundreds or thousands of eV, and then these pre-accelerated particles are further energized by betatron acceleration. This two-step process is similar to electron acceleration that occurs near reconnection regions in the magnetotail of Earth's magnetosphere during dipolarization events (Ashour-Abdalla et al., 2011). For the magnetospheric configuration and initial solar wind parameters corresponding to simulations 1 and 2, the maximum energy achieved in the magnetosphere by any particle for either case is ~ 25 keV.

This result for electron energies in Mercury's magnetosphere for the conditions found during simulations 1 and 2 is consistent with MESSENGER flyby data. A comparison of the electron energy distribution in the equatorial plane from simulation 1 is made with the data from the Energetic Particle Spectrometer (EPS) sensor and XRS instrument for flyby M1 in Fig. 3. It can be seen that the EPS sensor (top panel) detected no electrons in the energy range 36–65 keV, whereas the XRS instrument, which can indirectly detect 1–10 keV electrons (Slavin et al., 2008; Ho et al., this issue), showed increases at about the locations where the simulation shows the presence of \sim keV electrons that entered the magnetosphere. Most of these electrons have a sufficiently large pitch angle that they mirror bounce in the dipole-like magnetic field and move around the planet azimuthally due to radius of curvature and gradient B drifts, which for electrons is in the counterclockwise direction in the equatorial plane when viewed looking down from above the north pole. There is reasonable qualitative agreement between the simulation model results and the MESSENGER data for the first flyby case both in spatial location and energy for the XRS instrument (middle panel), as well as for the lack of high-energy electrons from the EPS sensor (top panel).

3.2. Electron precipitation flux and energy

As discussed above, about 5% of electrons that are launched from the solar wind enter the magnetosphere and precipitate directly onto the planetary surface. The precipitation flux for these electrons is shown for simulations 1 and 2 in Fig. 4. It can be seen that for both northward (S1, left panel) and southward IMF (S2, right panel), electron fluxes as large as 10^9 – 10^{10} $\text{cm}^{-2} \text{s}^{-1}$ are found at some locations. The locations of where electrons precipitate is quite different for simulations 1 and 2, which is due to the different magnetospheric topology that results from having either a northward or southward IMF. For the northward IMF case corresponding to M1 (upper panel), the strongest electron precipitation occurs at a very focused region at the high northern latitudes on the dayside and near the equator in the dawn sector, whereas for southward IMF (S2, lower panel), maximum precipitation fluxes tend to occur at the equator on the dawn-dayside region. There is also substantial precipitation in the northern hemisphere for S2, primarily due to the large radial IMF component (B_x), which tends to skew the reconnection region above the equator, even for southward IMF. For S1, precipitation tends to occur along a narrow region of open field lines, i.e., fields with one end connected to the planet and the other end connected to the solar wind, which occur at high latitudes near noon for northward IMF. In S2 (southward IMF), dayside reconnection occurs at lower latitudes over a broader region in longitude. Also in S2, when electrons pass through the reconnection region they tend to gain more energy with more spread in pitch and phase angle, which leads to a wider precipitation region in both latitude and longitude.

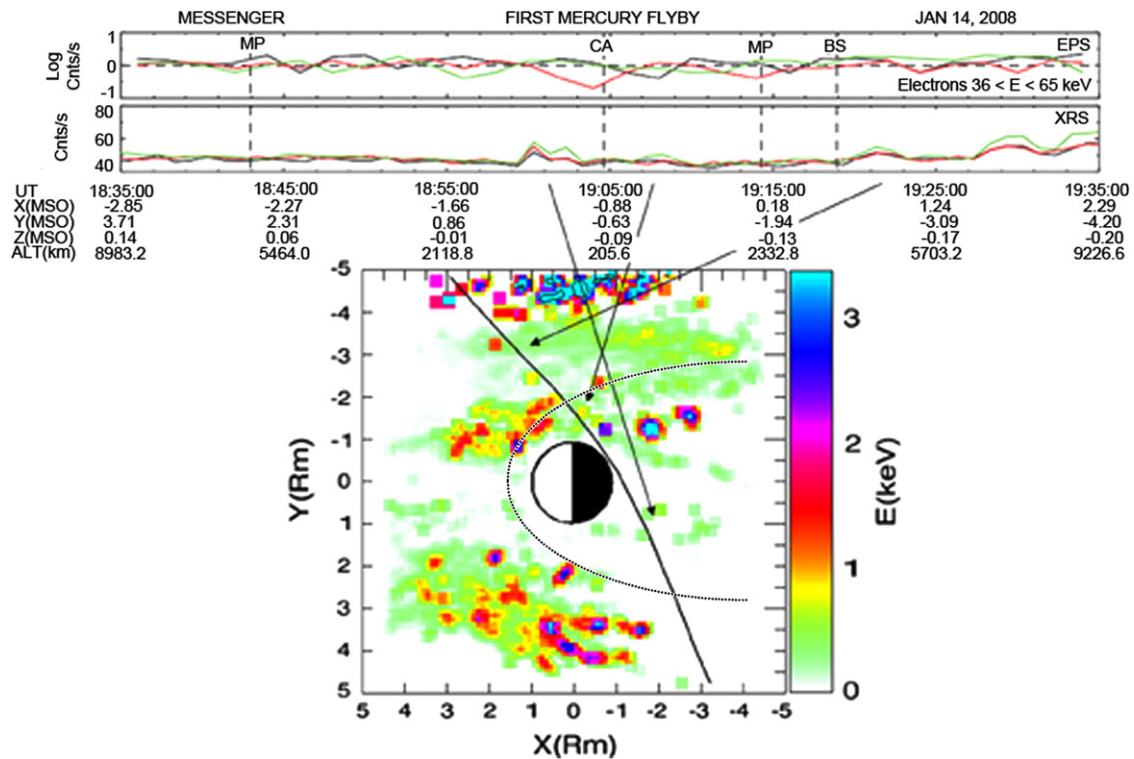


Fig. 3. The top two panels show electron count data during M1 from the EPS sensor and the XRS instrument, respectively, and the bottom panel shows the electron energy profiles in the equatorial plane for simulation 1 (S1). In the bottom panel the Sun is to the left, the solid curve shows MESSENGER's trajectory, and the dotted curve shows the approximate location of the magnetopause. Note that in the bottom panel the energy scale is saturated at 3 keV in contrast to the left panel of Fig. 2. The arrows show the approximate positions along the MESSENGER trajectory where observations were made at the given times.

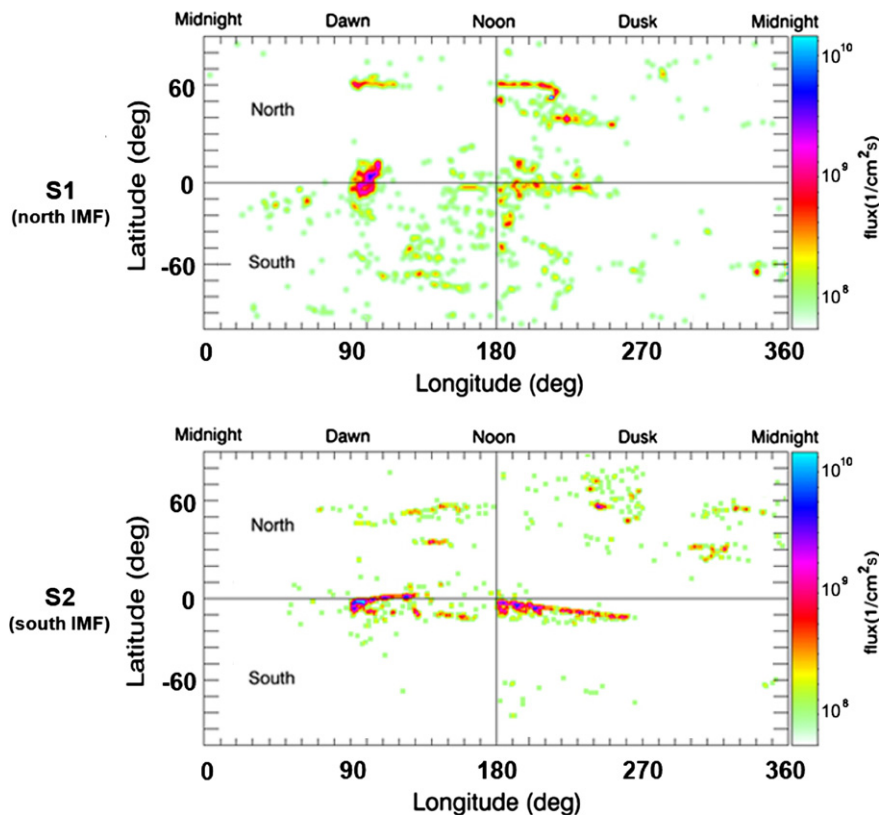


Fig. 4. Electron precipitation fluxes are shown for simulation 1 (S1) in the top panel and simulation 2 (S2) in the lower panel. Both panels show latitude versus longitude, with 0° latitude corresponding to the equator, 90° latitude the north pole, -90° latitude the south pole, 0°/360° longitude corresponding to midnight, 90° longitude dawn, 180° longitude noon, and 270° longitude dusk.

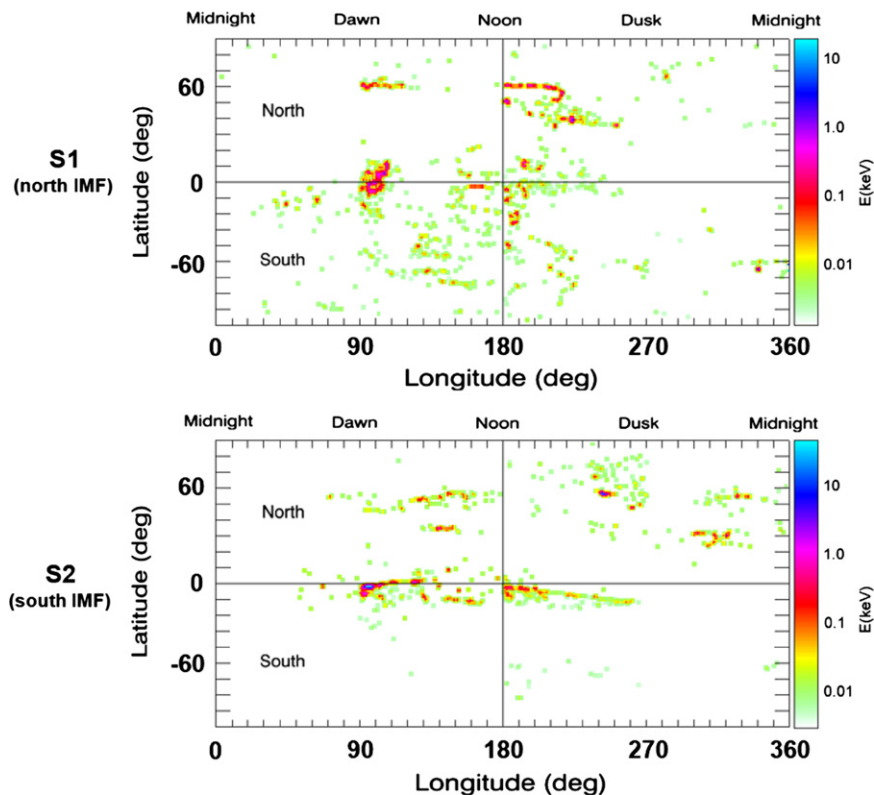


Fig. 5. Electron precipitation energies are shown for simulation 1 (S1) in the top panel and simulation 2 (S2) in the lower panel. Conventions for latitude and longitude follow those in Fig. 4.

The corresponding electron precipitation energies are shown for simulations 1 and 2 in Fig. 5, in the same format as Fig. 4, but color coded by energy on a log scale. Note that the two panels have a slightly different energy scale. On average the precipitating energies for S2 can be higher by a factor of 3 or more, a result similar to the equatorial energies seen in Fig. 2. The reason for the difference in precipitating energies is the same as for the equatorial energies, i.e., it is due to the difference in reconnection location and intensity for northward IMF (S1) and southward IMF (S2). Where the precipitation fluxes are the largest for S1, in the northern hemisphere near noon, the average precipitating energies are ~ 300 eV. For S2, the highest precipitation fluxes, which are near the dayside and dawnside equator, have average energies up to ~ 2 keV.

3.3. Electron-stimulated desorption as a source of Mercury's exosphere

The results found for the precipitating electron fluxes and energies can be used with recent experimental measurements concerning the release of neutrals and ions due to electron bombardment to estimate the contribution of ESD to Mercury's exosphere and surrounding ion cloud. McLain et al. (2011) examined electron-beam bombardment of simulated Mercury regolith targets using pulsed low-energy electron irradiation of Na- and K-bearing silicate glasses and found that direct desorption of H^+ , H_2^+ , O^+ , H_3O^+ , Na^+ , K^+ , and O_2^+ occurs. The estimated total cross-section for ESD at a typical surface temperature of 400 K is $> 10^{-19}$ cm² and represents an upper-limit yield between 10^{-4} and 10^{-5} ions/e⁻ for 200 eV electrons and between 10^{-3} and 10^{-4} ions/e⁻ for 2 keV electrons.

Using the results found here and integrating the fluxes over the area where precipitation occurs for the entire planet give $\sim 10^{26}$ precipitating electrons per second (approximately the

same for both northward and southward IMF), which, combined with the ESD yields found by McLain et al. (2011), give a value of 10^{21} – 10^{23} ions/s emitted from the planet. This result puts ESD on par with ion sputtering at Mercury as discussed by Killen et al. (2004), who quoted values for ion sputter yields between 6.0×10^{21} and 3.8×10^{24} ions/s. It should be noted that McLain et al. (2011) looked at surrogate silicates that may behave somewhat differently than the actual planetary materials. Although the physics of the desorption/removal process will be the same, the overall removal cross sections and neutral/ion branching ratios could be different.

4. Conclusions

A simulation study has been carried out to examine electron transport and acceleration in Mercury's magnetosphere for parameters that correspond approximately to the conditions that prevailed during the first two MESSENGER flybys of Mercury. One of the main differences in external conditions between the two flybys was that during M1 the IMF had a northern component, whereas during M2 the IMF had a southern component. In the simulation models all other parameters were taken to be identical in the two cases.

Concerning electron energies within Mercury's magnetosphere, the maximum energy achieved by any particle was about 25 keV for either case, and in the equatorial plane along the MESSENGER flyby trajectories the energies were about 1–10 keV. These results are in good agreement with measurements made by the EPS sensor, which did not record any flux enhancements for energies > 36 keV, and with those from the XRS instrument, which indirectly observed 1–10 keV electrons near the planet (Slavin et al., 2008; Ho et al., this issue). Due to more efficient reconnection for the case with southward IMF, the simulation

results showed that electron energies were on average several times higher than for the case with northward IMF, which had more localized, less efficient reconnection.

The simulations carried out here were for a constant IMF and solar wind pressure, and under the assumption that Mercury's magnetosphere was in quasi-equilibrium. The solar wind speed, taken to be 4 times the Alfvén speed (~ 450 km/s), would be considered average or on the slow side, compared to high solar wind speeds of > 600 km/s that have been observed (e.g., Burlaga, 2001; Baker et al., this issue). A highly variable IMF and/or a higher solar wind speed is expected to result in higher electron energies in Mercury's magnetosphere. A variable IMF can result in rapid changes in magnetic topology, stronger reconnection, and large inductive electric fields, all of which can energize electrons to higher energy values. Higher solar wind speed means a larger overall kinetic energy level of electrons (which varies as velocity squared), which ultimately can lead to higher energies in the magnetosphere. Mariner 10 data showed the presence of high-energy (> 35 keV) electrons, which may have been a result of a more active, higher-pressure solar wind, compared to the relatively quiet solar wind conditions that characterized the MESSENGER flybys. This inference may be supported by the presence of dipolarization events during the Mariner 10 measurements of high-energy electrons, whereas no similar dipolarization events were seen during the first two MESSENGER flybys. Dipolarization events are commonly observed in Earth's magnetotail during substorms as pulses of enhanced northward magnetic field ($B_z > 0$), which propagate earthward accompanied by high-energy ions and electrons (Ashour-Abdalla et al., 2009, 2011). As shown by Ashour-Abdalla et al. (2011), a combination of electron acceleration near the magnetotail reconnection region and then betatron acceleration in the dipolarization regions accounts for very high-energy electrons with energies of up to hundreds of keV during such events. The absence of such magnetic dipolarization events during MESSENGER's Mercury flybys is consistent with the observed lack of high-energy electrons (i.e., > 35 keV).

Maximum electron precipitation fluxes of $10^9 - 10^{10}$ $\text{cm}^{-2} \text{s}^{-1}$ were found in the simulation with energies ranging from a few hundred eV to \sim keV. For the case corresponding to M1, electron precipitation fluxes were the largest in a relatively narrow region in the northern hemisphere on the dawn dayside. For the case corresponding to M2, electron precipitation occurred over a much wider range in longitude, from noon around to the dawn side, very close to the equator, although there were flux enhancements in the northern hemisphere as well. Among the contributions to the uncertainties in obtaining the numerical values for the precipitating fluxes and energies are the solar wind speed, temperature, and density, which are used in the normalization factor that translates particle counts at the virtual detectors into densities, fluxes, and energies (Richard et al., 1994). Here a solar wind speed of 450 km/s, temperature of 20 eV, and density of 15 cm^{-3} were used. There are no *in situ* solar wind measurements available at the location of Mercury during the MESSENGER flybys, and these values are inferred from the observed location of the magnetopause boundary (e.g., Slavin et al., 2008, 2009), which can be used to calculate the solar wind pressure, and results from the ENLIL solar wind model (Baker et al., 2009, this issue). Interestingly, the ENLIL model results indicate that the solar wind density may be much higher than what is used here (up to 50 cm^{-3}). Higher solar wind densities in the normalization factor would result in even higher fluxes than found here. Thus the flux values found in this study could represent a lower limit.

The precipitating flux values and energies found in the simulations, along with recent experimental results concerning the release of neutrals and ions due to electron bombardment (McLain et al., 2011), indicate that electron-stimulated desorption

can play an important role in the formation of Mercury's exosphere and the heavy ion cloud that surrounds the planet. In particular, ESD, along with other mechanisms such as proton sputtering, photo-stimulated desorption, and impact vaporization, may complete the picture and account for the distribution and abundances of neutral species such as Na, Ca, and Mg, and ionized calcium observed in the vicinity of Mercury during the MESSENGER flybys (McClintock et al., 2008, 2009; Vervack et al., 2010). This premise will be examined in more detail in a future study quantifying the neutral and ionized emission and spatial distribution around Mercury due to ESD for the electron precipitation fluxes and the energies found here.

Acknowledgment

This work was supported by NASA MESSENGER grants NNX07AR62G, NNX07AV79G, and NNX09AD41G, NASA LWS Grant NNX09AJ73G, NASA Planetary Atmospheres Program NNG06-GG20G, contract ME09009 of the Czech Ministry of Education, and PECS contract 98068 from the European Space Agency. Computing was carried out on the NASA Advanced Supercomputing (NAS) Silicon Graphics Altix machine as part of the Columbia supercomputing system and the National Science Foundation (NSF) National Center for Atmospheric Research (NCAR) Frost Blue Gene supercomputing system. Global hybrid simulations used for this work were performed on the Amalka supercomputing facility at the Institute of Atmospheric Physics, Academy of Sciences of the Czech Republic.

References

- Anderson, B.J., Acuña, M.H., Korth, H., Purucker, M.E., Johnson, C.L., Slavin, J.A., Solomon, S.C., McNutt Jr., R.L., 2008. The structure of Mercury's magnetic field from MESSENGER's first flyby. *Science* 321, 82–85. doi:10.1126/science.1159081.
- Ashour-Abdalla, M., Berchem, J., Büchner, J., Zelenyi, L., 1993. Shaping of the magnetotail from the mantle: global and local structuring. *J. Geophys. Res.* 98, 5651–5676.
- Ashour-Abdalla, M., Zelenyi, L.M., Peromian, V., Richard, R.L., 1994. Consequences of magnetotail ion dynamics. *J. Geophys. Res.* 99, 14891–14916.
- Ashour-Abdalla, M., Bosqued, J.M., El-Alaoui, M., Peromian, V., Zhou, M., Richard, R.L., Walker, R.J., Runov, A., Angelopoulos, V., 2009. A simulation study of particle energization observed by THEMIS spacecraft during a substorm. *J. Geophys. Res.* 114, A09204. doi:10.1029/2009JA014126.
- Ashour-Abdalla, M., El-Alaoui, M., Schriver, D., Richard, R., Walker, R.J., Goldstein, M.L., Zhou, M., Kivelson, M.G., Hwang, K.-J., 2011. Observations and simulations of non-local acceleration of electrons in magnetotail magnetic reconnection events. *Nat. Phys.* 7, 360–365. doi:10.1038/nphys1903.
- Baker, D.N., Odstrcil, D., Anderson, B.J., Arge, C.N., Benna, M., Gloeckler, G., Raines, J.M., Schriver, D., Slavin, J.A., Solomon, S.C., Killen, R.M., Zurbuchen, T.H., 2009. Space environment of Mercury at the time of the first MESSENGER flyby: solar wind and interplanetary magnetic field modeling of upstream conditions. *J. Geophys. Res.* 114, A10101. doi:10.1029/2009JA014287.
- Baker, D.N., Odstrcil, D., Anderson, B.J., Arge, C.N., Benna, M., Gloeckler, G., Korth, H., Mayer, L.R., Raines, J.M., Schriver, D., Slavin, J.A., Solomon, S.C., Trávníček, P., Zurbuchen, T.H. The space environment of Mercury at the times of the second and third MESSENGER flybys. *Planet. Space Sci.*, this issue. doi:10.1016/j.pss.2011.01.018.
- Bida, T.A., Killen, R.M., Morgan, T.H., 2000. Discovery of calcium in Mercury's atmosphere. *Nature* 404, 159–161.
- Birn, J., Thomsen, M.F., Borovsky, J.E., Reeves, G.D., McComas, D.J., Belian, R.D., Hesse, M., 1998. Substorm electron injections: geosynchronous observations and test particle simulations. *J. Geophys. Res.* 103, 9235–9248.
- Blanco-Cano, X., Omid, N., Russell, C.T., 2003. Hybrid simulations of solar wind interaction with magnetized asteroids: comparison with Galileo observations near Gaspra and Ida. *J. Geophys. Res.* 108 (A5), 1216. doi:10.1029/2002JA009618.
- Brecht, S.H., 1990. Magnetic asymmetries of unmagnetized planets. *Geophys. Res. Lett.* 17, 1243–1246.
- Brecht, S.H., 1997. Hybrid simulations of the magnetic topology of Mars. *J. Geophys. Res.* 102, 4743–4750.
- Brecht, S.H., Ferrante, J.R., Luhmann, J.G., 1993. Three-dimensional simulations of the solar wind interaction with Mars. *J. Geophys. Res.* 98, 1345–1347.
- Brizard, A.J., Chan, A.A., 1999. Nonlinear relativistic gyrokinetic Vlasov–Maxwell equations. *Phys. Plasmas* 6, 4548–4558.

- Broadfoot, A.L., Shemanky, D.E., Kumar, S., 1976. Mariner 10: Mercury atmosphere. *Geophys. Res. Lett.* 3, 577–580.
- Büchner, J., Zelenyi, L.M., 1986. Deterministic chaos in the dynamics of charged particles near a magnetic field reversal. *Phys. Lett. A* 118, 395–399.
- Büchner, J., Zelenyi, L.M., 1989. Regular and chaotic charged particle motion in magnetotail-like field reversals. 1. Basic theory of trapped motion. *J. Geophys. Res.* 94, 11821–11842.
- Burlaga, L.F., 2001. Magnetic fields and plasmas in the inner heliosphere: Helios results. *Planet. Space Sci.* 49, 1619–1627.
- Convery, P.D., Schriver, D., Ashour-Abdalla, M., Richard, R.L., 2002. Wave-particle interactions associated with nongyrotropic distribution functions: a hybrid simulation study. *J. Geophys. Res.* 107, 1013. doi:10.1029/2001JA000160.
- Delamere, P.A., 2009. Hybrid code simulations of the solar wind interaction with Pluto. *J. Geophys. Res.* 114, A03220. doi:10.1029/2008JA013756.
- Delamere, P.A., Bagenal, F., 2004. Pluto's kinetic interaction with the solar wind. *Geophys. Res. Lett.* 31, L04807. doi:10.1029/2003GL018122.
- Delcourt, D.C., Sauvaud, J.A., Martin Jr., R.F., Moore, T.E., 1996. On the nonadiabatic precipitation of ions from the near-Earth plasma sheet. *J. Geophys. Res.* 101, 17409–17418.
- Delcourt, D.C., Seki, K., Terada, N., Miyoshi, Y., 2005. Electron dynamics during substorm dipolarization in Mercury's magnetosphere. *Ann. Geophys.* 23, 3389–3398.
- Domingue, D.L., Koehn, P.L., Killen, R.M., Sprague, A.L., Sarantos, M., Cheng, A.F., Bradley, E.T., McClintock, W.E., 2007. Mercury's atmosphere: a surface-bounded exosphere. *Space Sci. Rev.* 131, 161–186.
- Dubinin, E.M., Sauer, K., Lundin, R., Baumgartel, K., Bogdanov, A., 1996. Structuring of the transition region (plasma mantle) of the Martian magnetosphere. *Geophys. Res. Lett.* 23, 785–788.
- Dubinin, E.M., Sauer, K., Baumgartel, K., Srivasta, K., 1998. Multiple shocks near Mars. *Earth Planets Space* 50, 279–287.
- Dungey, J.W., 1989. Noise-free neutral sheets. In: Guyenne, T.D., Hunt, J.J. (Eds.), *Reconnection in Space Plasma*, Special Publication SP-285, vol. II. European Space Agency, Paris, France, pp. 15–19.
- Elkington, S.R., Hudson, M.K., Chan, A.A., 1999. Acceleration of relativistic electrons via drift-resonant interaction with toroidal-mode Pc-5 ULF oscillation. *Geophys. Res. Lett.* 26, 3273–3276.
- Elkington, S.R., Hudson, M.K., Chan, A.A., 2003. Resonant acceleration and diffusion of outer zone electrons in an asymmetric geomagnetic field. *J. Geophys. Res.* 108 (A3), 1116. doi:10.1029/2001JA009202.
- Hada, T., Kennel, C.F., 1985. Nonlinear evolution of slow waves in the solar wind. *J. Geophys. Res.* 90, 531–535.
- Hesse, M., Winske, D., Kuznetsova, M.M., 1995. Hybrid modeling of collisionless reconnection in two-dimensional current sheets. *J. Geophys. Res.* 100, 21815–21825.
- Ho, G.C., Starr, R.D., Gold, R.E., Krimigis, S.M., Slavin, J.A., Baker, D.N., Anderson, B.J., McNutt Jr., R.L., Nittler, L.R., Solomon, S.C. Observations of suprathermal electrons in Mercury's magnetosphere during the three MESSENGER flybys. *Planet. Space Sci.*, this issue. 10.1016/j.pss.2011.01.011.
- Hudson, M.K., Elkington, S.R., Lyon, J.G., Marchenko, V.A., Roth, I., Temerin, M., Gussenhoven, M.S., 1996. MHD/particle simulations of radiation belt formation during a storm sudden commencement. In: Lemaire, J.F., Heynderickx, D., Baker, D.N. (Eds.), *Radiation Belts: Models and Standards*, Geophys. Monograph Ser., vol. 97. American Geophysical Union, Washington, D.C., pp. 57–62.
- Hudson, M.K., Elkington, S.R., Lyon, J.G., Goodrich, C.C., Rosenberg, T.J., 1999. Simulation of radiation belt dynamics driven by solar wind variations. In: Burch, J.L., Carovillano, R.L., Antiochos, S.K. (Eds.), *Sun-Earth Plasma Connections*, Geophys. Monograph Ser., vol. 109. American Geophysical Union, Washington, D.C., pp. 171–182.
- Hudson, M.K., Elkington, S.R., Lyon, J.G., Goodrich, C.C., 2000. Increase in relativistic electron flux in the inner magnetosphere: ULF wave mode structure. *Adv. Space Res.* 25, 2327–2337.
- Hunten, D.M., Morgan, T.H., Schemansky, D.E., 1988. The Mercury atmosphere. In: Vilas, F., Chapman, C.R., Matthews, M.S. (Eds.), *Mercury*. University of Arizona Press, Tucson, Ariz., pp. 562–612.
- Jackson, D.J., Beard, D.B., 1977. The magnetic field of Mercury. *J. Geophys. Res.* 82, 2828–2836.
- Kallio, E., Wurz, P., Killen, R., McKenna-Lawlor, S., Milillo, A., Mura, A., Massetti, S., Orsini, S., Lammer, H., Janhunen, P., Ip, W.-H., 2008. On the impact of multiply charged heavy solar wind ions on the surface of Mercury, the Moon and Ceres. *Planet. Space Sci.* 56, 1506–1516.
- Killen, R.M., Ip, W.-H., 1999. The surface bounded atmospheres of Mercury and the Moon. *Rev. Geophys.* 37, 361–406.
- Killen, R.M., Potter, A.E., Reiff, P., Sarantos, M., Jackson, B.V., Hick, P., Giles, B., 2001. Evidence for space weather at Mercury. *J. Geophys. Res.* 106, 20509–20525.
- Killen, R.M., Sarantos, M., Potter, A.E., Reiff, P., 2004. Source rates and ion recycling rates for Na and K in Mercury's atmosphere. *Icarus* 171, 1–19.
- Kivelson, M.T., Russell, C.T., 1995. *Introduction to Space Physics*. Cambridge University Press, Cambridge, pp. 503–519.
- Krauss-Varban, D., Omid, N., 1995. Large-scale hybrid simulations of the magnetotail during reconnection. *Geophys. Res. Lett.* 22, 3271–3274.
- Kuznetsova, M.M., Hesse, M., Winske, D., 1996. Ion dynamics in a hybrid simulation of magnetotail reconnection. *J. Geophys. Res.* 101, 27351–27373.
- Leblanc, F., Delcourt, D., Johnson, R.E., 2003. Mercury's sodium exosphere: magnetospheric ion recycling. *J. Geophys. Res.* 108 (E12), 5136. doi:10.1029/2003JE002151.
- Leroy, M.M., Goodrich, C.C., Winske, D., Wu, C.S., Papadopoulos, K., 1981. Simulation of a perpendicular bow shock. *Geophys. Res. Lett.* 8, 1269–1272.
- Leroy, M.M., Winske, D., Goodrich, C.C., Wu, C.S., Papadopoulos, K., 1982. The structure of perpendicular bow shocks. *J. Geophys. Res.* 87, 5081–5094.
- Lin, Y., Swift, D.W., 1996. A two-dimensional hybrid simulation of the magnetotail reconnection layer. *J. Geophys. Res.* 101, 19859–19870.
- Lipatov, A.S., 2002. *The Hybrid Multiscale Simulation Technology*. Springer-Verlag, New York, 403 pp.
- Lipatov, A.S., Sauer, K., Baumgartel, K., 1997. 2.5D hybrid code simulation of the solar wind interaction with weak comets and related objects. *Adv. Space Res.* 20, 279–282.
- Lipatov, A.S., Motschmann, U., Bagdonat, T., 2002. 3-D hybrid simulations of the interaction of the solar wind with a weak comet. *Planet. Space Sci.* 50, 403–411.
- Lyons, L.R., Pridmore-Brown, D.C., 1990. Force balance near an X line in a collisionless plasma. *J. Geophys. Res.* 95, 20903–20909.
- Lyons, L.R., Pridmore-Brown, D.C., 1992. Force balance near an X line along which $\mathbf{E} \cdot \mathbf{B} < 0$. *J. Geophys. Res.* 97, 2955–2960.
- Madey, T.E., Yakshinskiy, B.V., Ageev, V.N., Johnson, R.E., 1998. Desorption of alkali atoms and ions from oxide surfaces: relevance to origins of Na and K in atmospheres of Mercury and the Moon. *J. Geophys. Res.* 103, 5873–5887.
- Matthews, A., 1994. Current advance method and cyclic leapfrog for 2D multispecies hybrid plasma simulations. *J. Comput. Phys.* 112, 102–116.
- McClintock, W.E., Bradley, E.T., Vervack Jr., R.J., Killen, R.M., Sprague, A.L., Izenberg, N.R., Solomon, S.C., 2008. Mercury's exosphere: observations during MESSENGER's first Mercury flyby. *Science* 321, 92–94. doi:10.1126/science.1159467.
- McClintock, W.E., Vervack Jr., R.J., Bradley, E.T., Killen, R.M., Mouawad, N., Sprague, A.L., Burger, M.H., Solomon, S.C., Izenberg, N.R., 2009. MESSENGER observations of Mercury's atmosphere: detection of magnesium and distribution of constituents. *Science* 324, 610–613. doi:10.1126/science.1172525.
- McLain, J., Grieves, G.A., Sprague, A.L., Schriver, D., Travnicek, P., Orlando, T.M., 2011. Electron-stimulated desorption of silicates: a potential source for ions in Mercury's space environment. *J. Geophys. Res.* 116, E03007. doi:10.1029/2010JE003714.
- Milillo, A., Wurz, P., Orsini, S., Delcourt, D., Kallio, E., Killen, R.M., Lammer, H., Massetti, S., Mura, A., Barabash, S., Cremonese, G., Daglis, I.A., De Angelis, E., Di Lellis, A.M., Livi, S., Mangano, V., Torkar, K., 2005. Surface-exosphere-magnetosphere system of Mercury. *Space Sci. Rev.* 117, 397–444.
- Morgan, T.H., Killen, R.M., 1997. A non-stoichiometric model of the composition of the atmospheres of Mercury and the Moon. *Planet. Space Sci.* 45, 81–97.
- Ness, N.F., Behannon, K.W., Lepping, R.P., Whang, Y.C., Schatten, K.H., 1974. Magnetic field observations near Mercury: preliminary results from Mariner 10. *Science* 185, 151–160.
- Ness, N.F., Behannon, K.W., Lepping, R.P., 1975. The magnetic field of Mercury. *J. Geophys. Res.* 80, 2708–2716.
- Ness, N.F., Behannon, K.W., Lepping, R.P., Whang, Y.C., 1976. Observations of Mercury's magnetic field. *Icarus* 28, 479–488.
- Northrop, T.G., 1963. *The Adiabatic Motion of Charged Particles*. Interscience Publishers, New York, 109 pp.
- Omura, Y., Ashour-Abdalla, M., Quest, K., Gendrin, R., 1985. Heating of thermal helium in the equatorial magnetosphere: a simulation study. *J. Geophys. Res.* 90, 8281–8292.
- Orlando, T.M., Sprague, A.L., Grieves, G.A., Schriver, D., Travnicek, P.M., McLain, J.L., Starr, R.D., 2010. Electron stimulated desorption as a source mechanism for ions in Mercury's space environment. *Lunar Planet. Sci.* 41, abstract 2246.
- Perry, K.L., Hudson, M.K., Elkington, S.R., 2005. Incorporating spectral characteristics of Pc5 waves into three-dimensional radiation belt modeling and the diffusion of relativistic electrons. *J. Geophys. Res.* 110, A03215. doi:10.1029/2004JA010760.
- Potter, A.E., Morgan, T.H., 1985. Discovery of sodium in the atmosphere of Mercury. *Science* 229, 651–653.
- Potter, A.E., Killen, R.M., Morgan, T.H., 1999. Rapid changes in the sodium exosphere of Mercury. *Planet. Space Sci.* 47, 1441–1448.
- Press, W.H., Flannery, B.P., Teukolsky, S.A., Vetterling, W.T., 1989. *Numerical Recipes: The Art of Scientific Computing*. Cambridge University Press, Cambridge, 702 pp.
- Richard, R.L., Walker, R.J., Ashour-Abdalla, M., 1994. The population of the magnetosphere by solar wind ions when the interplanetary magnetic field is northward. *Geophys. Res. Lett.* 21, 2455–2458.
- Russell, C.T., Baker, D.N., Slavin, J.A., 1988. The magnetosphere of Mercury. In: Vilas, F., Chapman, C.R., Matthews, M.S. (Eds.), *Mercury*. University of Arizona Press, Tucson, Ariz., pp. 514–561.
- Schriver, D., Ashour-Abdalla, M., 1994. Ion and electron distributions near an X-line. In: Kan, J.R., Craven, J.D., Akasofu, S.-I. (Eds.), *Second International Conference on Substorms (ICS-2)*. Geophysical Institute, University of Alaska, Fairbanks, Alaska, pp. 503–509.
- Schriver, D., Ashour-Abdalla, M., 1995. Signatures of electron acceleration in the magnetotail. In: Chang, T., Jasperse, J.R. (Eds.), *Physics of Space Plasmas (1993)*. Center for Theoretical Geo/Cosmo Plasma Physics, MIT, Cambridge, Mass, pp. 403–421.
- Schriver, D., Ashour-Abdalla, M., Richard, R.L., 1998. On the origin of the ion-electron temperature difference in the plasma sheet. *J. Geophys. Res.* 103, 14879–14895.
- Schriver, D., Ashour-Abdalla, M., Zelenyi, L., Gombosi, T., Ridley, A., De Zeeuw, D., Toth, G., Monostori, G., 2005. Modeling the kinetic transport of electrons through the Earth's global magnetosphere. In: *Proceedings of the 7th*

- International School/Symposium for Space Simulations. Research Institute for Sustainable Humanosphere, Kyoto University, Kyoto, Japan, pp. 345–346.
- Shimazu, H., 1999. Three-dimensional hybrid simulation of magnetized plasma flow around an obstacle. *Earth Planets Space* 51, 383–393.
- Shimazu, H., 2001. Three-dimensional hybrid simulation of solar wind interaction with unmagnetized planets. *J. Geophys. Res.* 106, 8333–8342.
- Simpson, J.A., Eraker, J.H., Lampert, J.E., Walpole, P.H., 1974. Electrons and protons accelerated in Mercury's magnetosphere. *Science* 185, 160–166.
- Slavin, J.A., Acuña, M.H., Anderson, B.J., Baker, D.N., Benna, M., Gloeckler, G., Gold, R.E., Ho, G.C., Killen, R.M., Korth, H., Krimigis, S.M., McNutt Jr., R.L., Raines, J.M., Schriver, D., Solomon, S.C., Starr, R., Trávníček, P., Zurbuchen, T.H., 2008. Mercury's magnetosphere after MESSENGER's first flyby. *Science* 321, 85–89. doi:10.1126/science.1159040.
- Slavin, J.A., Acuña, M.H., Anderson, B.J., Baker, D.N., Benna, M., Boardsen, S., Gloeckler, G., Gold, R.E., Ho, G.C., Korth, H., Krimigis, S.M., McNutt Jr., R.L., Raines, J.M., Sarantos, M., Schriver, D., Solomon, S.C., Trávníček, P., Zurbuchen, T.H., 2009. MESSENGER observations of magnetic reconnection in Mercury's magnetosphere. *Science* 324, 606–610. doi:10.1126/science.1172011.
- Slavin, J.A., Acuña, M.H., Anderson, B.J., Baker, D.N., Benna, M., Boardsen, S., Gloeckler, G., Gold, R.E., Ho, G.C., Korth, H., Krimigis, S.M., McNutt Jr., R.L., Raines, J.M., Sarantos, M., Schriver, D., Solomon, S.C., Trávníček, P., Zurbuchen, T.H., 2010. MESSENGER observations of extreme loading and unloading of Mercury's magnetic tail. *Science* 329, 665–668. doi:10.1126/science.1188067.
- Smets, R., Delcourt, D., Fontaine, D., Martin Jr., R.F., 1996. Structure of electron and ion distribution functions near a reconnection line. *J. Geophys. Res.* 101, 24837–24845.
- Solomon, S.C., McNutt Jr., R.L., Watters, T.R., Lawrence, D.J., Feldman, W.C., Head, J.W., Krimigis, S.M., Murchie, S.L., Phillips, R.J., Slavin, J.A., Zuber, M.T., 2008. Return to Mercury: a global perspective on MESSENGER's first Mercury flyby. *Science* 321, 59–62. doi:10.1126/science.1159706.
- Speiser, T.W., 1965. Particle trajectories in model current sheets, 1. Analytical solutions. *J. Geophys. Res.* 70, 4219–4226.
- Sprague, A.L., Kozlowski, R.W.H., Hunten, D.M., Schneider, N.M., Domingue, D.L., Wells, W.K., Schmitt, W., Fink, U., 1997. Distribution and abundance of sodium in Mercury's atmosphere, 1985–1988. *Icarus* 129, 506–527.
- Swift, D.W., 1995. Use of a hybrid code to model the Earth's magnetosphere. *Geophys. Res. Lett.* 22, 311–314.
- Swift, D.W., Lee, L.C., 1983. Rotational discontinuities and the structure of the magnetopause. *J. Geophys. Res.* 88, 111–124.
- Tanaka, T., 1985. Simulations of heavy ion heating by electromagnetic ion cyclotron waves driven by proton temperature anisotropies. *J. Geophys. Res.* 90, 6459–6468.
- Trávníček, P., Hellinger, P., Schriver, D., 2007. Structure of Mercury's magnetosphere for different pressure of the solar wind: three dimensional hybrid simulations. *Geophys. Res. Lett.* 34, L05104. doi:10.1029/2006GL028518.
- Trávníček, P.M., Hellinger, P., Schriver, D., Hercik, D., Slavin, J.A., Anderson, B.J., 2009. Kinetic instabilities in Mercury's magnetosphere: three-dimensional simulation results. *Geophys. Res. Lett.* 36, L07104. doi:10.1029/2008GL036630.
- Trávníček, P.M., Hellinger, P., Schriver, D., Hercik, D., Anderson, B.J., Sarantos, M., Slavin, J.A., Zurbuchen, T., 2010. Mercury's magnetosphere—solar wind interaction for northward and southward interplanetary magnetic field: hybrid simulation results. *Icarus* 209, 11–22. doi:10.1016/j.icarus.2010.01.008.
- Vervack Jr., R.J., McClintock, W.E., Killen, R.M., Sprague, A.L., Anderson, B.J., Burger, M.H., Bradley, E.T., Mouawad, N., Solomon, S.C., Izenberg, N.R., 2010. Mercury's complex exosphere: results from MESSENGER's third flyby. *Science* 329, 672–675.
- Whang, Y.C., 1977. Magnetospheric magnetic field of Mercury. *J. Geophys. Res.* 82, 1024–1030.
- Winske, D., 1985. Hybrid simulation codes with application to shocks and upstream waves. *Space Sci. Rev.* 42, 53–66.
- Winske, D., Leroy, M.M., 1984. Diffuse ions produced by electromagnetic ion beam instabilities. *J. Geophys. Res.* 89, 2673–2688.
- Winske, D., Yin, L., Omid, N., Karimabadi, H., Quest, K., 2003. Hybrid simulation codes: past, present and future—a tutorial. In: Büchner, J., Dum, C.T., Scholer, M. (Eds.), *Space Plasma Simulation, Lecture Notes in Physics*, vol. 615. Springer-Verlag, Berlin, pp. 136–165.
- Zelenyi, L.M., Galeev, A.A., Kennel, C.F., 1990. Ion precipitation from the inner plasma sheet due to stochastic diffusion. *J. Geophys. Res.* 95, 3871–3882.
- Zurbuchen, T.H., Raines, J.M., Gloeckler, G., Krimigis, S.M., Slavin, J.A., Koehn, P.L., Killen, R.M., Sprague, A.L., McNutt Jr., R.L., Solomon, S.C., 2008. MESSENGER observations of the composition of Mercury's ionized exosphere and plasma environment. *Science* 321, 90–92. doi:10.1126/science.1159314.